

Bondi-Hoyle-Lyttleton accretion flow in a stratified layer

F. J. Sánchez-Salcedo[★]

Universidad Nacional Autónoma de México, Instituto de Astronomía, P.O. Box 70-264, Ciudad Universitaria, 04510, Mexico City, Mexico

Accepted XXX. Received YYY; in original form ZZZ

ABSTRACT

We compute the density and velocity profiles along the tail induced by a body of mass M , embedded in the midplane of a vertically-stratified media with scaleheight H , adopting a one-dimensional model as in the Bondi-Hoyle-Lyttleton problem. In analogy to what occurs in the case of a homogeneous medium, there exist a family of solutions that satisfy the boundary conditions. A shooting method is employed to isolate those solutions that fulfill a specific set of physical and mathematical constraints. The tail is found to be both densest and slowest when the scaleheight H is equal to the gravitational radius $\xi_0 \equiv GM/v_0^2$, where v_0 its relative velocity with respect to the medium. The location of the stagnation point is evaluated as a function of H and ξ_0 , and an empirical fitting formula is provided. While the distance to the stagnation point is maximized when $H \simeq \xi_0$, the mass accretion rate attains its maximum value for $H \ll \xi_0$ at fixed surface density. When instead the midplane density is held constant and H is varied, the accretion rate hardly changes once H exceeds about $2\xi_0$. Additionally, we investigate how both the drag force resulting from mass accretion and the gravitational drag arising from its tail depend on H/ξ_0 . We highlight how the effect of varying the degree of mixing in the tail influences the resulting drag force. Finally, for the particular case of an infinitely thin layer, we provide a simple analytical solution, which may serve as a useful pedagogical reference.

Key words: accretion, accretion discs – black hole physics – hydrodynamics – ISM: general – stars: winds, outflows.

1 INTRODUCTION

Gas accretion onto a gravitating object remains an active area of research in astrophysics with applications including galaxy formation, star formation, compact objects and stellar binary systems (see Edgar 2004, for a review). The steady-state model for spherical accretion proposed by Bondi (1952) and the Bondi, Hoyle and Lyttleton (BHL) description for accretion onto moving objects (Hoyle & Lyttleton 1939; Bondi & Hoyle 1944) serve as fundamental reference models. These theoretical approaches provide a basis for comparison with the outcomes of numerical simulations (e.g., Ruffert 1996) and are also useful when additional effects are introduced, such as other gravitational potentials (e.g., Lin & Murray 2007; Ciotti & Pellegrini 2017; Kaaz et al. 2019), a rigid boundary around the body (Thun et al. 2016; Prust & Bildsten 2024), magnetic fields (e.g. Igumenshchev & Narayan 2002; Toropina et al. 2012; Sánchez-Salcedo 2012; Lee et al. 2014), fluid instabilities (Beckmann et al. 2018), binaries (Antoni et al. 2019), a low angular momentum (Proga & Begelman 2003) or a turbulent (Krumholz et al. 2006; Burleigh et al. 2017; Lescaudron et al. 2023) medium.

Most studies on the BHL problem assume a large-scale, three-dimensional medium. In realistic astrophysical systems, density or velocity gradients may be important (e.g., Livio et al. 1986). In a spherical system with a radial density gradient, accretors in circular orbit feels a transverse density gradient; this occurs for instance in binary systems (e.g., MacLeod & Ramírez-Ruiz 2015; Xu & Stone 2019). On the other hand, there exist many situations where bodies

are embedded in vertically-stratified discs. For example, planets in protoplanetary discs, or black holes and stars within the accretion disc of AGNs. In the case of Bondi accretion, vertical stratification is expected to reduce the accretion rate relative to the homogeneous case (e.g., Dittmann et al. 2021; Zhou et al. 2024; Chen et al. 2025). It should be noted, however, that embedded bodies, even if they are on circular orbits, accrete according to Bondi’s prescription only when their masses lie below the thermal mass (e.g. Choksi et al. 2023). In particular, the resulting accretion flow onto gap-opening planets departs significantly from the assumptions underlying Bondi accretion (e.g. Rosenthal et al. 2020; Li et al. 2023).

When planets, stars or black holes are on eccentric or inclined orbits, they typically move supersonically relative to the surrounding gas (e.g., Muto et al. 2011; Rein 2012; Xiang-Gruess & Papaloizou 2013), placing them under the BHL accretion model. An interesting scenario for BHL accretion within a disc arises in the aftermath of the merger of two spiral galaxies, where intermediate-mass and supermassive black holes migrate towards the galactic nucleus and can form an eccentric black-hole binary. This binary could be embedded within the nuclear gaseous disc of the merged galaxies (see Mayer et al. 2007, for the case of equal-mass galaxies). If the orbital eccentricities of these accretors are $\gtrsim 2h$, where h is the disc’s aspect ratio, they will move supersonically with respect to the gas in the disc (e.g., Muto et al. 2011). Black holes can move also supersonically if they are counterrotating with respect to the AGN accretion disc (Secunda et al. 2021; Sánchez-Salcedo & Santillán 2025).

A distinct case of BHL accretion in a disc emerges in a binary system formed by a high-mass Be star and a neutron star or black hole. Due to its rapid rotation, the Be star may develop a decretion

[★] E-mail: jsanchez@astro.unam.mx

disc (Hanuschik 1996; Carciofi 2011; Martin et al. 2025). In eccentric binary systems, the neutron star (or black hole) can accrete material from the disc when it approaches periastron (e.g., Negueruela & Okazaki 2001; Negueruela et al. 2001; Okasaki et al. 2002; Okazaki et al. 2013; Li et al. 2021).

There are two key physical quantities of interest that one aims to estimate: the mass accretion rate onto the perturber and the drag force. The contribution of the far-field wake to the drag force can be computed using linear theory. Some authors have extended the linear-theory drag force formula from a homogeneous medium to a disc geometry by simply setting the maximum impact parameter to $\sim H$, the scaleheight of the disc (e.g., Artymowicz et al. 1993; Xiang-Gruess & Papaloizou 2013). Muto et al. (2011) compute the drag force on a body moving supersonically in a planar 2D medium in linear theory and apply it to study the migration and eccentricity damping timescales of planets in eccentric orbits (see also Sánchez-Salcedo 2019; Ida et al. 2020). Vicente et al. (2019) also use linear theory to compute the drag force and the wake generated by a body moving through a constant-density slab, imposing Dirichlet conditions on the upper and lower surfaces. One limitation of linear theory is the ambiguity in choosing the minimum impact parameter, because the interaction becomes nonlinear at sufficiently small distances from the perturber.

The ambiguity in the minimum impact radius can be resolved either by relying on numerical simulations (e.g., Bernal & Sánchez-Salcedo 2013; Suzuguchi et al. 2024) or by modelling the nonlinear regime directly. Cantó et al. (2013, hereafter C13) analytically evaluate the accretion mass rate and the drag force (including the contribution from the nonlinear inner part of the wake) acting on a body embedded in a vertically stratified medium. In a thin layer, they find that the total drag force is independent of the object's velocity. For a thick layer, they determine the minimum and maximum impact parameters in the Coulomb logarithm. However, while C13 also employ a ballistic approach and assume a zero thickness wake, as in the BHL model, they additionally assume no mixing of wake material, in contrast with the BHL prescription, which assumes perfect mixing. In the present work, using the classical BHL assumptions, we compute the tail density, accretion rate and drag force on a supersonic body moving in the midplane of a stratified medium.

The paper is organized as follows. Section 2 provides an overview of the BHL equations in the classical homogeneous medium within the BHL framework of line accretion. In Section 3, we extend the BHL approach for a stratified medium, and obtain the continuity and momentum equations in the steady state. Section 4 focuses on the solution in the limit of a very thin layer, a case for which a simple analytical solution can be derived. In Section 5, we present the results obtained for layers of arbitrary vertical thickness. A clarifying remark regarding the far-field wake's contribution to the drag force is presented in Section 6. Finally, the conclusions are summarized in Section 7.

2 THE CLASSICAL BHL PROBLEM: AN OVERVIEW

Since a homogeneous medium is a special case of a stratified medium with zero gradient, it is instructive to first consider the classical homogeneous case. We treat the Hoyle & Lyttleton (1939) and Bondi & Hoyle (1944) models in separate subsections, since they are not equivalent and may yield different mass accretion rates.

2.1 The analysis of Hoyle & Lyttleton (1939)

To study the accretion flow induced by a gravitating body of mass M travelling through a cold homogeneous medium, Hoyle & Lyttleton (1939) used a ballistic description of the gas and thus neglected the forces due to gas pressure.

Consider a coordinate system centred on the object, such that the gas approaches the body from large distances ($x \rightarrow -\infty$) with velocity $v_0 \hat{x}$, where $v_0 > 0$. Within this ballistic approximation, the incoming particles move on hyperbolic orbits. The velocity components along the x -axis and in the perpendicular direction, for a streamline characterized by the impact parameter ξ are given by

$$v_x = v_0 \left(1 + \frac{1}{\xi} |\sin \theta| \right), \quad (1)$$

and

$$v_y = -\frac{v_0}{\xi} (1 + \cos \theta), \quad (2)$$

where θ is the polar angle measured from the downstream axis, such that $\theta = 0$ corresponds to the direction immediately behind the perturber.

These expressions describe the flow along a streamline until it intersects the x -axis. A streamline with impact parameter ξ intersects the x axis at a distance

$$x_\xi = \frac{\xi^2}{2\xi_0} \quad (3)$$

from the perturber. Here $\xi_0 \equiv r_{\text{HL}}/2 = GM/v_0^2$, being r_{HL} the Hoyle-Lyttleton accretion radius $r_{\text{HL}} \equiv 2GM/v_0^2$. Hoyle & Lyttleton (1939) argued that gas will collide in the tail behind the star and will lose kinetic energy because the y -component of the velocity thermalize. They positioned that streamlines satisfying

$$\frac{1}{2} v_x^2 - \frac{GM}{x_\xi} < 0 \quad (4)$$

will have insufficient energy to escape from the gravitational potential of the star and therefore will be accreted onto the star. Since $v_x = v_0$ in the x -axis (Eq. 1, with $\theta = 0$), the above equation implies that all streamlines with impact parameter less than $2\xi_0 = r_{\text{HL}}$ will be accreted. The mass accretion rate is therefore given by

$$\dot{M}_{\text{HL}} = 4\pi \rho_0 v_0 \xi_0^2 = \frac{4\pi \rho_0 G^2 M^2}{v_0^3}. \quad (5)$$

The above accretion rate is commonly refer to the Hoyle-Lyttleton accretion rate.

Bondi & Hoyle (1944) proposed a more refined description of the accretion flow. They argued that the Hoyle-Lyttleton accretion rate should be regarded as an upper limit. In the following subsection, we present the equations governing the accretion tail in a homogeneous 3D medium.

2.2 The BHL analysis for the tail in the case of a homogeneous 3D medium

Bondi & Hoyle (1944) also neglected the pressure forces and assumed that, when streamlines intersect, they form a high-density filament from the body downflow, i.e. at $x > 0$. If energy is rapidly irradiated, this accretion column or tail can be considered as infinitesimally thin, with linear mass density $\mu(x)$ and velocity $v(x)$. Thus, $v(x)$ represents the velocity of the material in the tail relative to the object. In fact, Bondi & Hoyle (1944) assumed that in the accretion column,

all the material at a given x moves with the same velocity $v(x)$ (see upper panel in Figure 1).

To determine $\mu(x)$ and $v(x)$, Bondi & Hoyle (1944) derived the steady-state continuity and momentum equations governing the structure of the tail. These equations are given by

$$\frac{\partial(\mu v)}{\partial x} = 2\pi\xi_0\rho_0v_0, \quad (6)$$

and

$$\frac{\partial(\mu v^2)}{\partial x} = 2\pi\xi_0\rho_0v_0^2 - \frac{GM\mu}{x^2}, \quad (7)$$

where ρ_0 is the density of the ambient medium (e.g., Bondi & Hoyle 1944; Lyttleton 1972; Edgar 2004; Matsuda et al. 2015; Raga et al. 2022). The right-hand side of Equation (6) and the first term on the right-hand side of Equation (7) represent the rates of mass and momentum flux per unit length, being incorporated into the tail, respectively. The second term in the right-hand side of Equation (7) accounts for the gravitational force exerted by the object on the tail. In this paper, we use the term ‘BHL model’ to refer to the solutions of Equations (6)-(7) in a homogeneous medium, and to their extension to a stratified medium derived in Section 3.

To solve the differential equations (6) and (7) for $\mu(x)$ and $v(x)$, Bondi & Hoyle (1944) imposed three boundary conditions: (I) there is a stagnation point at $x = x_0$, i.e. $v = 0$ at $x = x_0$, (II) the velocity v far downstream approach to v_0 , and (III) $dv/dx \geq 0$ for all $x > 0$. Lyttleton (1972) showed that there are infinitely many solutions that satisfy the boundary conditions imposed by Bondi & Hoyle (1944) and additionally found a class of ‘slow’ solutions for which $v \rightarrow 0$ when $x \rightarrow \infty$. The different types of solutions including the effect of the pressure in the accretion column was studied by Horedt (2000). Edgar (2004) showed that the condition (III) implies that $x_0 \geq \xi_0$, i.e. $\tilde{x}_0 \equiv x_0/\xi_0 \geq 1$. Matsuda et al. (2015) removed the problem of the non-uniqueness of the solution by assuming three additional requirements: (IV) $d\mu/dx \geq 0$ for all $x > 0$, (V) $d^2v/dx^2 \leq 0$ at all $x > 0$ and (VI) $d^2\mu/dx^2 \leq 0$. They found that condition (IV) implies $1.325 < \tilde{x}_0 < 2$; condition (V) yields $1.395 < \tilde{x}_0 < 1.768$; and condition (VI) constrains \tilde{x}_0 to $1.617 < \tilde{x}_0 < 1.627$. Therefore, they conclude that the stagnation point in the 3D (axisymmetric) case is located at $\tilde{x}_0 \simeq 1.62$.

Recently, Raga et al. (2022) solve the time-dependent equations using a finite-difference method until the solution reaches a stationary state, obtaining $\tilde{x}_0 \simeq 1.51$. Their solution resembles that of Matsuda et al. (2015). Raga et al. (2022) also provide an analytical fit to the solution.

The value of the stagnation point \tilde{x}_0 is physically relevant because it determines the mass accretion rate. From Eq. (3), a streamline intersecting the x -axis at x_0 has an impact parameter $\xi_{\text{acc}} = \sqrt{2\xi_0x_0}$. Since $r_{\text{HL}} = 2\xi_0$, this reduces to $\xi_{\text{acc}} = r_{\text{HL}}$ only when $x_0 = 2\xi_0$; otherwise $\xi_{\text{acc}} \neq r_{\text{HL}}$. The mass accretion rate is given by

$$\dot{M} = \pi\rho_0v_0\xi_{\text{acc}}^2 = \left(\frac{\tilde{x}_0}{2}\right)\dot{M}_{\text{HL}}, \quad (8)$$

where \dot{M}_{HL} is the nominal Hoyle-Lyttleton accretion rate given in Eq. (5). Consequently, if $\tilde{x}_0 = 1.62$, as derived by Matsuda et al. (2015), \dot{M} is reduced by a factor 0.81 relative to \dot{M}_{HL} .

In principle, numerical simulations can adopt more realistic physical conditions and yield a more reliable estimate of the accretion rate. Horedt (2000) provide a compilation of the values of \tilde{x}_0 reported in the literature (see also Edgar 2004).

To evaluate the gravitational drag force experienced by M , we only require $\mu(x)$. Although the free-streaming flow induces changes in the ambient density (see Eqs. 7 and 8 in Cantó et al. 2011, hereafter

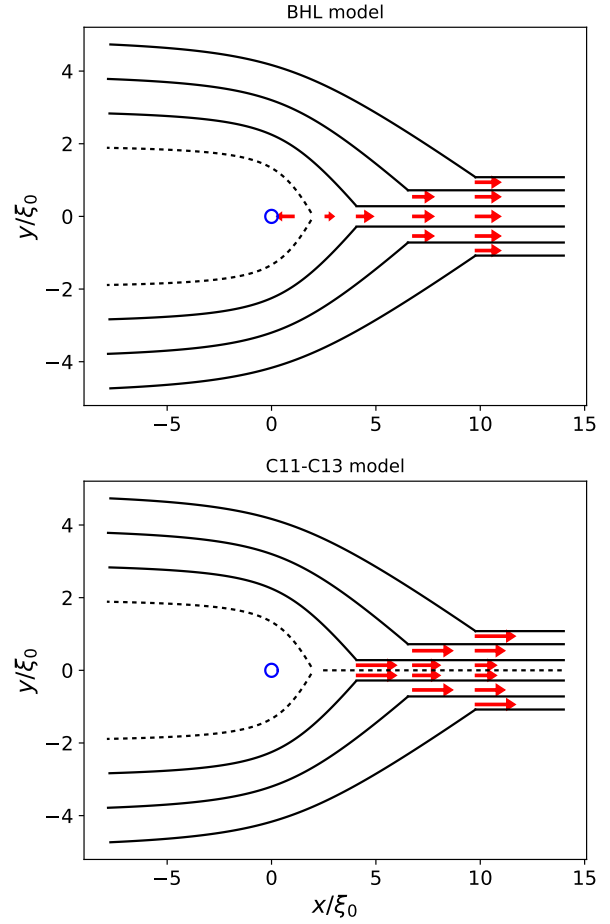


Figure 1. Schematic of the flow (not to scale) in the BHL approach (top panel) and in the C11-C13 model (bottom panel). The solid lines indicate the streamlines and the red arrows represent the velocity in the tail. The dotted lines correspond to the streamline with impact parameter $2\xi_0$. The tail is slower in the BHL model. While the flow in the tail is assumed plane-parallel in both models, it presents shear in the C11-C13 model. Streamlines with impact parameter $\leq 2\xi_0$ are assumed to entry into the accretor, but they are not modelled in the C11-C13 model.

C11), the density outside the thin tail does not contribute to the drag force on the body. This follows directly from Equation (1). When a gas parcel reaches the symmetry axis ($\theta = 0$), its x -component of the velocity remains v_0 . Momentum conservation along the x -direction then ensures that the net x -force exerted by an entire streamline tube is zero¹.

¹ We caution that integrating the gravitational force from gas in the free-streaming flow over a volume that contains incomplete streamline tubes (for example, a cylinder aligned with the x -axis) will yield a nonzero force.

2.3 Underlying assumptions: BHL versus C11 and C13

As mentioned in the previous subsection, the BHL model assumes that all material entering the tail mixes instantaneously and adopts a common velocity, with the associated dissipation of energy. Under this assumption, the velocity in the tail depends only on the distance along the symmetry axis and is uniform across any transverse cross section. [Bondi & Hoyle \(1944\)](#) justified this approximation by arguing that small transverse velocity components generate circulation that efficiently mixes the gas within the cross section. For this assumption to hold, the associated transverse mixing timescale must be shorter than the characteristic time on which velocity gradients are produced by gravity. This assumption is unlikely to be valid within the Hoyle-Lyttleton accretion radius, where the velocity field inside the Mach cone exhibits a dependence on θ (e.g., [Bisnovatyi-Kogan et al. 1979](#)). However, it may provide a reasonable description of the flow farther downstream from the accretor, where the velocity field varies primarily along the axis (e.g., [Ruffert 1996](#)).

By contrast with the mixing assumption, [C11](#) and [C13](#) assume that once the transverse velocity components, v_y and v_z , are thermalized, the total energy along each streamline is conserved. As a result, the longitudinal component v_x retains information about the fluid parcel's original impact parameter, leading to a sheared velocity profile within the tail (see Figure 1). We will refer to the assumptions presented in references [C11](#) and [C13](#) as the C11–C13 model.

The calculation of the mass accretion rate in [C11](#) is identical to that used by [Hoyle & Lyttleton \(1939\)](#) and described in Subsection 2.1. Consequently, in the [C11](#) model, the accretion rate is equal to \dot{M}_{HL} .

The assumptions underlying the BHL and C11–C13 are extreme limits, so the true physical configuration is expected to be bracketed by these two limiting cases. A conceptual caveat of [Hoyle & Lyttleton \(1939\)](#) and C11–C13 models concerns the motion of gas with impact parameters $\leq 2\xi_0$. As discussed in [C11](#), these models do not provide a clear description of how such gas initially moves away from the accretor before subsequently reverses direction and falls back toward the body.

3 BHL EQUATIONS IN A GAUSSIAN AMBIENT MEDIUM

We consider a gaseous medium stratified along the vertical direction z , with a density profile given by

$$\rho(z) = \rho_0 \exp\left(-\frac{z^2}{2H^2}\right), \quad (9)$$

where ρ_0 is the volume density at the midplane ($z = 0$) and H is the scaleheight. The surface density of the layer is $\Sigma = \sqrt{2\pi}\rho_0 H$. In the midplane, the accretor, which is represented as a point mass M , is moving hypersonically at velocity $-v_0 \hat{x}$ relative to the ambient medium. As in Section 2, we take a coordinate system with the object at the centre, such that the gas upstream at $x \rightarrow -\infty$ moves with velocity $v_0 \hat{x}$. Note that, within the ballistic approximation, Equations (1)–(3) also remain valid in a vertically stratified medium.

Before outlining the BHL equations for $\mu(x)$ and $v(x)$ in the stratified case, it is important to emphasize the limitations of the idealized BHL assumptions when applied to a body embedded in a disc. In particular, the BHL framework assumes negligible gas pressure and vanishing angular momentum in the accretion flow. The ballistic approximation is justified in the free-streaming region provided that the body moves supersonically relative to the gas, a condition satisfied for eccentricities $e > 2h$ (e.g., [Papaloizou 2002](#); [Muto et al. 2011](#); [Ida et al. 2020](#)). Within the downstream tail, pressure forces become

progressively less important as cooling becomes more efficient, i.e. as the sound speed in the tail tends to zero ([Raga et al. 2022](#)); this constitutes the most restrictive limitation of the BHL assumptions (see Section 6). On the other hand, background shear is negligible when the epicycle velocity exceeds the sound speed, so that the flow near the accretor is more nearly ballistic than shear dominated (e.g., [Chen et al. 2022](#)). Indeed, in the supersonic regime ($e > 2h$) and for a body with an orbital radius r , the response timescale of the dynamical-friction wake, $\sim H/(er\Omega)$, is shorter than the local shear timescale $\sim \Omega^{-1}$ ([Papaloizou 2002](#)), allowing the gas to react before differential rotation distorts the flow.

3.1 Continuity and momentum equations

To compute the mass flux feeding the tail, we first evaluate the mass flux per unit impact parameter, which, for the density distribution of Equation (9) reads

$$\begin{aligned} \frac{d\dot{m}}{d\xi} &= 4\rho_0 v_0 \xi \int_0^{\pi/2} \exp\left(-\frac{\xi^2 \sin^2 \theta}{2H^2}\right) d\theta \\ &= 2\pi\rho_0 v_0 \xi I_0\left(\frac{\xi^2}{4H^2}\right) \exp\left(-\frac{\xi^2}{4H^2}\right), \end{aligned} \quad (10)$$

where $I_0(y)$ is the modified Bessel function of the first kind of order zero. The amount of mass that is incorporated to the tail per unit distance, along $x > 0$, is given by

$$\Lambda(x) = \frac{d\dot{m}}{d\xi} \frac{d\xi}{dx}. \quad (11)$$

Combining Eqs. (3) and (10), we obtain

$$\Lambda(x) = 2\pi\xi_0 \rho_0 v_0 I_0\left(\frac{\xi_0 x}{2H^2}\right) \exp\left(-\frac{\xi_0 x}{2H^2}\right). \quad (12)$$

In the 1D approximation, the continuity equation is

$$\frac{\partial \mu}{\partial t} + \frac{\partial}{\partial x}(\mu v) = \Lambda. \quad (13)$$

We recall that $\mu(x, t)$ is the linear mass density and $v(x, t)$ the velocity along the infinitesimally thin tail behind the accretor. On the other hand, the momentum equation is given by

$$\frac{\partial}{\partial t}(\mu v) + \frac{\partial}{\partial x}(\mu v^2) = \Lambda v_0 - \frac{GM\mu}{x^2}. \quad (14)$$

It is convenient to rewrite the above two equations in terms of dimensionless quantities $\tilde{x} \equiv x/\xi_0$, $\tilde{\mu} = \mu/(\sqrt{2\pi}\Sigma\xi_0)$ and $\tilde{t} \equiv tv_0/\xi_0$. The resulting equations are

$$\frac{\partial \tilde{\mu}}{\partial \tilde{t}} + \frac{\partial}{\partial \tilde{x}}(\tilde{\mu}\tilde{v}) = \frac{1}{\tilde{H}} I_0\left(\frac{\tilde{x}}{2\tilde{H}^2}\right) \exp\left(-\frac{\tilde{x}}{2\tilde{H}^2}\right), \quad (15)$$

and

$$\frac{\partial}{\partial \tilde{t}}(\tilde{\mu}\tilde{v}) + \frac{\partial}{\partial \tilde{x}}(\tilde{\mu}\tilde{v}^2) = \frac{1}{\tilde{H}} I_0\left(\frac{\tilde{x}}{2\tilde{H}^2}\right) \exp\left(-\frac{\tilde{x}}{2\tilde{H}^2}\right) - \frac{\tilde{\mu}}{\tilde{x}^2}, \quad (16)$$

where $\tilde{H} \equiv H/\xi_0$.

3.2 Steady-state equations

In the steady state, Equations (15) and (16) are simplified to

$$\frac{\partial}{\partial \tilde{x}}(\tilde{\mu}\tilde{v}) = \frac{1}{\tilde{H}} I_0\left(\frac{\tilde{x}}{2\tilde{H}^2}\right) \exp\left(-\frac{\tilde{x}}{2\tilde{H}^2}\right), \quad (17)$$

and

$$\frac{\partial}{\partial \tilde{x}}(\tilde{\mu}\tilde{v}^2) = \frac{1}{\tilde{H}} I_0\left(\frac{\tilde{x}}{2\tilde{H}^2}\right) \exp\left(-\frac{\tilde{x}}{2\tilde{H}^2}\right) - \frac{\tilde{\mu}}{\tilde{x}^2}. \quad (18)$$

Equations (17) and (18) are the extensions of Equations (6) and (7) to a Gaussian-stratified medium. We next combine Eqs. (17) and (18) to obtain a differential equation for \tilde{v} independent of $\tilde{\mu}$.

The above equation (18) can be written as

$$\tilde{v} \frac{d\tilde{\mu}\tilde{v}}{d\tilde{x}} + \tilde{\mu}\tilde{v} \frac{d\tilde{v}}{d\tilde{x}} = \frac{1}{\tilde{H}} I_0(s) e^{-s} - \frac{\tilde{\mu}}{\tilde{x}^2} \quad (19)$$

where $s \equiv \tilde{x}/(2\tilde{H}^2)$. Substituting $\partial(\tilde{\mu}\tilde{v})/d\tilde{x}$ from Eq. (17) into Eq. (19), we obtain

$$\tilde{\mu}\tilde{v} \frac{d\tilde{v}}{d\tilde{x}} = \frac{1 - \tilde{v}}{\tilde{H}} I_0(s) e^{-s} - \frac{\tilde{\mu}}{\tilde{x}^2}. \quad (20)$$

In order to eliminate the dependence on $\tilde{\mu}$ in Equation (20), we integrate Equation (17), which yields

$$\tilde{\mu}\tilde{v} = 2\tilde{H}(F(s) - F_0), \quad (21)$$

with

$$F(s) \equiv se^{-s} [I_0(s) + I_1(s)], \quad (22)$$

$F_0 \equiv F(s_0)$ and $s_0 \equiv \tilde{x}_0/(2\tilde{H}^2)$. From Eq. (21) we see that the velocity v is zero at a distance \tilde{x}_0 and thus it corresponds to the stagnation point.

Finally, using Eq. (21) into Eq. (20), we obtain

$$\frac{d\tilde{v}}{d\tilde{x}} = \frac{(1 - \tilde{v})I_0(s)e^{-s}}{2\tilde{H}^2[F(s) - F_0]} - \frac{1}{\tilde{x}^2\tilde{v}}. \quad (23)$$

This differential equation for \tilde{v} does not explicitly depend on $\tilde{\mu}$, but does depend on \tilde{x}_0 through F_0 . This equation has a critical point at $s = s_0$ (or $\tilde{x} = \tilde{x}_0$). Before examining the solution in the vicinity of this point, which we undertake in the next subsection, we demonstrate that, in the limit of a homogeneous medium, the equation simplifies to the standard BHL equation.

The case of a homogeneous medium corresponds to the limit of very large \tilde{H} . In this limit, both s and s_0 are very small so that we can expand $I_0(s)e^{-s} = 1 - s + \mathcal{O}(s^2)$, $I_1(s)e^{-s} = s/2 + \mathcal{O}(s^2)$ and $F(s) = s + \mathcal{O}(s^2)$ in Equations (21) and (23), to obtain

$$\tilde{\mu}\tilde{v} = \frac{1}{\tilde{H}}(\tilde{x} - \tilde{x}_0), \quad (24)$$

and

$$\frac{d\tilde{v}}{d\tilde{x}} = \frac{1 - \tilde{v}}{\tilde{x} - \tilde{x}_0} - \frac{1}{\tilde{x}^2\tilde{v}}. \quad (25)$$

In the homogeneous 3D case, the conventional normalization for μ is $\mu_* = \mu/(2\pi\rho_0\zeta_0^2)$. In these units, Equation (24) implies

$$\mu_*\tilde{v} = \tilde{x} - \tilde{x}_0. \quad (26)$$

Equations (25) and (26) correspond to the Equations (8) in Bondi & Hoyle (1944) for the homogeneous 3D case.

3.3 Solution behaviour near the critical point

It is possible to determine $\tilde{\mu}$ and $d\tilde{v}/d\tilde{x}$ at the critical point \tilde{x}_0 as follows. In a neighbourhood of \tilde{x}_0 , we have

$$\tilde{v} \simeq (\tilde{x} - \tilde{x}_0) \frac{d\tilde{v}}{d\tilde{x}} \bigg|_{\tilde{x}_0}. \quad (27)$$

Combining Eq. (21) and (27), it holds that

$$\tilde{\mu}\tilde{v} \simeq \tilde{\mu}_0(\tilde{x} - \tilde{x}_0) \frac{d\tilde{v}}{d\tilde{x}} \bigg|_{\tilde{x}_0} \simeq 2\tilde{H}(F(s) - F_0), \quad (28)$$

where $\tilde{\mu}_0 \equiv \tilde{\mu}(\tilde{x}_0)$. By substituting Eq. (23) into Eq. (28), it is simple to show that

$$\frac{\tilde{\mu}_0^2}{\tilde{x}_0^2} - \frac{\tilde{\mu}_0}{\tilde{H}} I_0(s_0) e^{-s_0} = -4\tilde{H}^2 \lim_{\tilde{x} \rightarrow \tilde{x}_0} \frac{[F(s) - F_0]^2}{\tilde{x} - \tilde{x}_0}. \quad (29)$$

Since the limit in the RHS of Equation (29) is zero, the linear density at \tilde{x}_0 is

$$\tilde{\mu}_0 = \frac{1}{\tilde{H}} \tilde{x}_0^2 I_0(s_0) e^{-s_0}. \quad (30)$$

It is worth noting that in the above equations, \tilde{x}_0 implicitly depends on \tilde{H} .

Now we are going to evaluate $d\tilde{v}/d\tilde{x}$ at the critical point. By expanding $F(s) \simeq F(s_0) + F'(s_0)(s - s_0)$ (where the prime indicates derivative respect to s), Equation (28) can be recast as

$$\tilde{\mu}_0 \frac{d\tilde{v}}{d\tilde{x}} \bigg|_{\tilde{x}_0} = \frac{1}{\tilde{H}} \frac{dF}{ds} \bigg|_{s_0}. \quad (31)$$

Noting that

$$\frac{dF}{ds} \bigg|_{s_0} = e^{-s_0} I_0(s_0), \quad (32)$$

and using Eq. (30), we get the simple relation

$$\frac{d\tilde{v}}{d\tilde{x}} \bigg|_{\tilde{x}_0} = \frac{1}{\tilde{x}_0^2}. \quad (33)$$

4 INFINITELY THIN LAYER

We now specialize to the case of an infinitely thin layer (2D planar case): $\tilde{H} \ll 1$ and $\tilde{H}^2 \ll \tilde{x}$. The latter condition implies $s \rightarrow 0$. In this limit, Equations (21), (23) and (30) become

$$\tilde{\mu}\tilde{v} = \frac{2}{\sqrt{\pi}}(\sqrt{\tilde{x}} - \sqrt{\tilde{x}_0}), \quad (34)$$

$$\frac{d\tilde{v}}{d\tilde{x}} = \frac{1 - \tilde{v}}{2(\tilde{x} - \sqrt{\tilde{x}_0}\tilde{x})} - \frac{1}{\tilde{x}^2\tilde{v}}, \quad (35)$$

and

$$\tilde{\mu}(\tilde{x}_0) = \frac{\tilde{x}_0^{3/2}}{\sqrt{\pi}}. \quad (36)$$

Equations (34), (35), and (36) were previously derived by Soker (1990), apart from some differences in factors due to the use of different variable normalization. However, as far as we know, analytical solutions seem to have been overlooked. After some algebraic manipulation, we find that the following expressions for $\tilde{\mu}$ and \tilde{v} provide a simple analytical solution to Equations (34)-(36)

$$\tilde{\mu}(\tilde{x}) = 2\sqrt{\frac{\tilde{x}}{\pi}}, \quad (37)$$

$$\tilde{v}(\tilde{x}) = 1 - \sqrt{\frac{2}{\tilde{x}}}. \quad (38)$$

This solution satisfies all the conditions (I to VI), outlined in Section 2. Therefore, it is a physically acceptable solution for BHL tail, within the simplifying assumptions of the model.

Clearly, the critical point for this particular solution is $\tilde{x}_0 = 2$. While 2D planar simulations have been also conducted by many authors (e.g., Anzer et al. 1987; Matsuda et al. 1987; Taam & Fryxell 1988; Matsuda et al. 1991; Blondin 2013), a large fraction of them

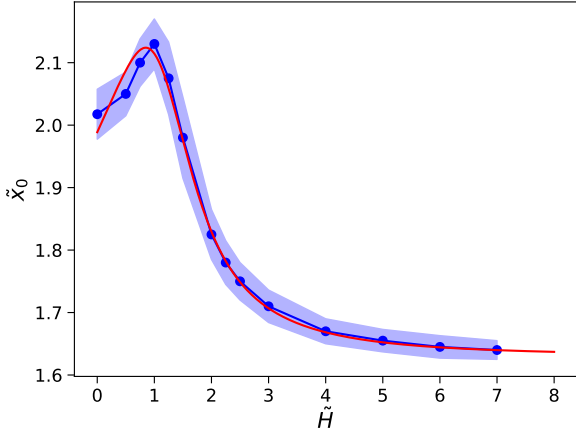


Figure 2. \tilde{x}_0 versus \tilde{H} . The blue band includes those values of \tilde{x}_0 that satisfy conditions (I)-(VI). The dots indicate the central value in that interval. The red line represents the analytical fit given in Eq. (43).

focus on inhomogeneous media and they do not report the position of the stagnation point.

Once x_0 is known, the accretion radius can be derived from Eq. (3), yielding $\xi_{\text{acc}} = \sqrt{2}\xi_0 x_0 = 2\xi_0$. It is remarkable that this value coincides with that derived by C11 and C13 using different assumptions. The accretion radius in the 2D planar case appears slightly larger than in the 3D case, where it typically ranges from $1.74\xi_0$ (Raga et al. 2022) to $1.8\xi_0$ (Matsuda et al. 2015).

The mass accretion rate in the 2D planar case is

$$\dot{M} = 2\xi_{\text{acc}} \Sigma v_0 = \frac{4GM\Sigma}{v_0}. \quad (39)$$

This value of \dot{M} matches the result obtained by C13.

The accretion of mass produces a drag force, F_{acc} , given by $\dot{M}v_0 = 4GM\Sigma$ on the accretor. In addition, the tail exerts a gravitational force F_g given by

$$F_g = GM \int_{x_0}^{x_{\text{max}}} \frac{\mu}{x^2} dx. \quad (40)$$

Replacing Eq. (37) into the above equation and taking $x_{\text{max}} = \infty$, we find

$$F_g = 2\sqrt{2}GM\Sigma\xi_0^{1/2} \int_{2\xi_0}^{\infty} x^{-3/2} dx = 4GM\Sigma. \quad (41)$$

Therefore, the total drag force is $F_T = F_{\text{acc}} + F_g = 8GM\Sigma$.

While the value of F_{acc} is identical to the value derived in C13, the magnitude of F_g is slightly different. C13 find $F_g = 2(\pi - 2)GM$, which is smaller by a factor of 0.57 compared to the value obtained here under BHL assumptions. We attribute this discrepancy to the inherently dissipative nature of the BHL (see Section 2), which results in a denser and slower tail compared to the C11-C13 model.

5 DISC WITH ARBITRARY H

As with Equation (25) derived by Bondi & Hoyle (1944) for a 3D homogeneous medium, Equation (23) also admits an infinite number of solutions that satisfy the boundary conditions. To find solutions to Eq. (23) that satisfy conditions (I)-(VI), we proceeded as follows. For a given pair of parameters \tilde{H} and \tilde{x}_0 , we integrated Eq. (23)

inwards from $\tilde{x} = 10$ to $\tilde{x}_0 + 0.02$, applying an explicit fourth-order Runge-Kutta method. A shooting approach was employed, in which the initial velocity at $\tilde{x} = 10$ was adjusted to identify solutions (if any exist) that fulfill conditions (I)-(VI) for the chosen values of \tilde{H} and \tilde{x}_0 . As a result, we identify a narrow region in the (\tilde{H}, \tilde{x}_0) plane within which physically admissible solutions at $\tilde{x} \geq \tilde{x}_0$ exist. To continue the integration inward, we smoothly pass through the critical point by taking advantage of the fact that the functional form

$$\tilde{v}(\tilde{x}) = 1 - \left(\frac{\tilde{x}_0}{\tilde{x}} \right)^{1/\tilde{x}_0} \quad (42)$$

satisfies Equation (33) and, in addition, it matches the exact solution in the infinitely thin layer (see Equation 38). Moreover, Raga et al. (2022) show that Equation (42) also provides a good fit to the solution in the homogeneous case. Thus, the functional form in Eq. (42) is well-suited to describe the BHL flow close to the critical point. Specifically, we use Eq. (42) to compute \tilde{v} at $\tilde{x}_0 - 0.02$, which serves as the initial velocity for the inward integration down to $\tilde{x} = 0.19$, carried out via the Runge-Kutta method. Finally, we verify that the resulting solution $\tilde{v}(\tilde{x})$ satisfies conditions (I)-(VI) in the whole interval $[0.19, 10]$ under consideration.

The narrow domain, delineating the viable combinations of \tilde{H} and \tilde{x}_0 , is shown in Figure 2. It is remarkable that \tilde{x}_0 has a maximum at $\tilde{H} \simeq 1$. At large \tilde{H} , \tilde{x}_0 tends to 1.62, the value obtained for the homogeneous medium by Matsuda et al. (2015), as expected. The value of \tilde{x}_0 at the centre of the interval can be fitted by the function:

$$\tilde{x}_0(\tilde{H}) = 1.63 + \frac{1}{3} \exp\left(-\frac{4\tilde{H}^2}{5}\right) + \frac{(\tilde{H} + 0.2)^{8/5}}{\tilde{H}^4 + 3}. \quad (43)$$

Figure 3 shows $\tilde{v}(\tilde{x})$ and $\tilde{\mu}(\tilde{x})$ for some values of \tilde{H} . For each \tilde{H} , the corresponding \tilde{x}_0 was chosen as the central value, indicated by the dots in Fig. 2². This Figure shows that, at least beyond $\tilde{x} = 2$, $\tilde{v}(\tilde{x})$ increases as \tilde{H} increases, provided $\tilde{H} > 1$. At a fixed \tilde{x} , the tail is slowest for $\tilde{H} = 1$. This behaviour is illustrated in the upper panel of Fig. 4, where we see that \tilde{v} at $\tilde{x} = 10$ is not a monotonic increasing function of \tilde{H} , but instead exhibits a minimum at $\tilde{H} = 1$. This behaviour is consistent with $\tilde{v}(\tilde{x})$ satisfying Equation (42). Indeed, we have verified that $\tilde{v}(\tilde{x})$ closely adheres to this equation at $\tilde{x} > \tilde{x}_0$. The tail is slowest for $\tilde{H} = 1$ because \tilde{x}_0 attains its maximum at that value of \tilde{H} (see Figure 2).

In the inner region, at $\tilde{x} < \tilde{x}_0$, the deviation of $\tilde{v}(\tilde{x})$ from Equation (42) is clearly visible in the lower panel of Fig. 4. The values of \tilde{v} at $\tilde{x} = 0.19$ obtained from the numerical solution differ significantly from those predicted by Eq. (42), except for $\tilde{H} = 0$ and $\tilde{H} = 2$, where Equation (42) provides an excellent approximation within the interval under consideration ($0.19 \leq \tilde{x} \leq 10$). The accuracy of Eq. (42) for $\tilde{H} = 0$ is expected, as it represents an exact solution for $\tilde{H} = 0$ and $\tilde{x}_0 = 2$, as demonstrated in Section 4.

While both the middle and lower panels of Figure 3 display $\tilde{\mu}$ versus \tilde{x} , they do so using different units. In the middle panel, we normalize to $\sqrt{2\pi}\Sigma\xi_0$, which is useful when exploring situations where \tilde{H} is varied while Σ is held constant. In this sense, the middle panel shows that at a given value of Σ , the BHL tail is densest for $\tilde{H} \simeq 1$, i.e. $H \simeq \xi_0$. Note that the curves of $\tilde{\mu}$ versus \tilde{x} in the middle panel can intersect.

² We note that, given \tilde{H} and the central value of \tilde{x}_0 , there exists a narrow interval of values for \tilde{v} at $\tilde{x} = 10$ (the initial value in the shooting method) for which the solutions satisfy conditions (I)-(VI). However, this interval is so narrow (with a width of approximately 0.002) that the corresponding solution curves appear indistinguishable in Figure 3. This ambiguity in the value of \tilde{v} at $\tilde{x} = 10$ is less than the size of the symbols in the upper panel of Figure 4.

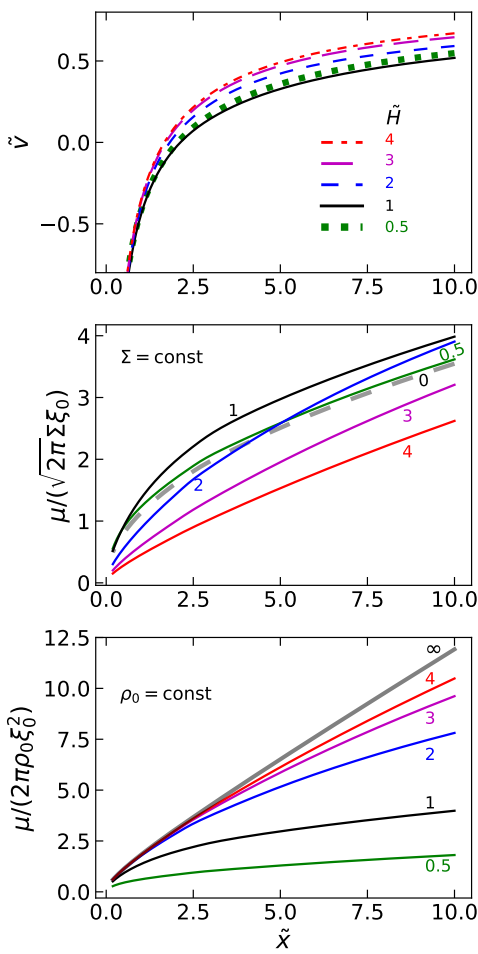


Figure 3. Dimensionless velocity \tilde{v} (upper panel) and linear density μ , normalized to $\sqrt{2\pi}\Sigma\xi_0$ in the middle panel, and to $2\pi\rho_0\xi_0^2$ in the lower panel, shown for different values of \tilde{H} indicated on each curve. For a given \tilde{H} , the value of \tilde{x}_0 was chosen as the central point of the blue band in Figure 2.

The lower panel is useful for examining how the linear density μ depends on the layer thickness when the volume density in the midplane remains fixed. As \tilde{H} increases, the curves asymptotically approach to the solution corresponding to the classical homogeneous medium (ie. case $\tilde{H} \rightarrow \infty$). It is apparent that the tail formed by an accretor in a thin layer is less dense than in a thick layer. While $\tilde{\mu}$ changes by nearly a factor of 2 when \tilde{H} increases from 1 to 2, it varies by only a factor of 1.18 when \tilde{H} increases from 2 to 3.

The mass accretion rate onto the body can be evaluated as the mass flow rate with impact parameter less than $\xi_{\text{acc}} \equiv \sqrt{2}\xi_0x_0$. More specifically,

$$\dot{M} = \int_0^{\xi_{\text{acc}}} \frac{d\dot{m}}{d\xi} d\xi = 2\pi\tilde{x}_0\rho_0v_0\xi_0^2 e^{-s_0} [I_0(s_0) + I_1(s_0)], \quad (44)$$

with $d\dot{m}/d\xi$ given in Equation (10). Figure 5 shows \dot{M} as a function of \tilde{H} using two normalizations. If Σ is held constant and \tilde{H} is varied, the

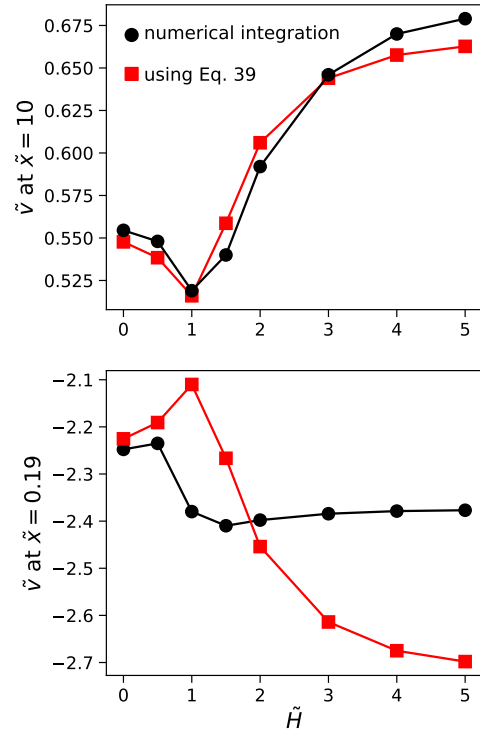


Figure 4. \tilde{v} at $\tilde{x} = 10$ (top panel) and at $\tilde{x} = 0.19$ (bottom panel) as a function of \tilde{H} in the solutions given in Figure 3 (black circles), together with the predicted values using Equation (42) with the corresponding values of \tilde{x}_0 (red squares).

maximum accretion rate occurs for $\tilde{H} = 0$. At large \tilde{H} , \dot{M} decreases because the volume density at the midplane, where the accretor is embedded, decreases as $\rho_0 = \Sigma/(\sqrt{2\pi}H) \propto H^{-1}$. An analytical fit of \dot{M} versus \tilde{H} yields the following result

$$\frac{\dot{M}}{\sqrt{2\pi}\Sigma v_0\xi_0} = \frac{2.9}{0.63\tilde{H}^{3/2} + 1.9} + 0.3(\tilde{H} + 0.2)e^{-\tilde{H}^2/2}. \quad (45)$$

Conversely, when ρ_0 is fixed and only \tilde{H} is varied, \dot{M} remains roughly constant beyond $\tilde{H} \simeq 2$ (see lower panel in Fig. 5). Below this value, \dot{M} decreases with decreasing \tilde{H} due to the reduced mass of the layer ($\Sigma \propto H$). In Figure 5, we also show the accretion rate predicted by the C13 model. It agrees with the BHL value for $\tilde{H} \lesssim 2$, but exceeds it by about 25% at large \tilde{H} values. The lower panel reveals that, at large \tilde{H} , the dimensionless accretion rates converge to 0.81 for the BHL model and to unity for the C13 model, as described in Sections 2.2 and 2.3.

Once $\mu(x)$ is known, we can compute the gravitational drag F_g using Equation (40). The total drag F_T will be $F_g + F_{\text{acc}}$, with $F_{\text{acc}} = \dot{M}v_0$. Figure 6 shows F_g and F_T as a function of \tilde{H} , for $x_{\text{max}} = 15\xi_0$ and $50\xi_0$. The left upper panel of Fig. 6 indicates that, if ξ_0 and Σ are both fixed, then F_g has a maximum at $\sim 1.5\tilde{H}$. For values larger than $1.5\tilde{H}$, F_g decreases monotonically. The lower panels show F_g and F_T normalized to $4\pi\rho_0(GM)^2/v_0^2$. As expected, if ρ_0 is kept constant and \tilde{H} increases, F_g increases as we have more material in the surrounding medium to be incorporated into the tail.

The shape of F_g as a function of \tilde{H} resembles that found in C13

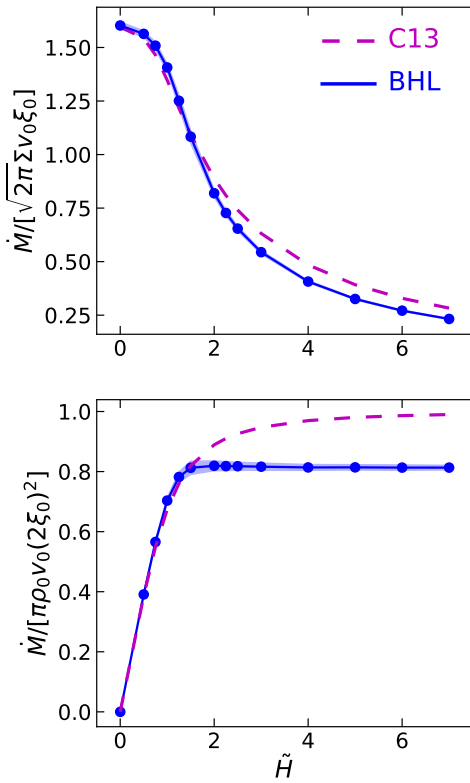


Figure 5. Mass accretion rate as a function of \tilde{H} . In the top panel, the accretion rate is normalized to $\sqrt{2}\pi\Sigma v_0 \xi_0$, whereas it is normalized to $\pi\rho_0 v_0 (2\xi_0)^2$ in the bottom panel. The solid curves correspond to the BHL model whereas the dashed lines for C13 model.

(see Figure 6). However, as in the $\tilde{H} = 0$ case, F_g is nearly twice as large as in the C13 model. Nevertheless, because F_{acc} is similar in both approaches, the total drag from the BHL tail is about 30% larger than in C13.

For accretors embedded in accretion discs on (quasi-)elliptical orbits, the timescales for radial migration and eccentricity damping can be estimated using a local approximation, in which F_T is evaluated pointwise along the orbit. This analysis is presented in the Appendix, where we also compare the results with previous studies that address the high-eccentricity regime.

To conclude this section, we compare the BHL predictions with the simulations of C13. These simulations consist of four 3D simulations with Mach number $\mathcal{M} \equiv v_0/c_s \geq 5$ and different values of \tilde{H} . The computational domain extends from $-7.5\xi_0$ to $7.5\xi_0$ in the direction of motion, so that $\tilde{x}_{\text{max}} = 7.5$. Figure 7 compares the simulated mass accretion rates \dot{M} and the total drag forces F_T with the corresponding BHL predictions. The BHL model reproduces the mass accretion rate accurately. Its estimates of F_T in models B, C, and D, all of which satisfy $\tilde{H} \leq \sqrt{2}\xi_0$, also agree reasonably well with the simulations. In contrast, for model A (nearly homogeneous case), the BHL model underestimates the drag force by a factor of about 1.4.³

³ The C13-model also underestimates F_T . Although C13 report good agree-

6 FAR-FIELD GRAVITATIONAL DRAG

The most significant limitation of BHL framework is that it neglects pressure effects. In the previous sections, we have compared two models that share this approximation but differ in their assumptions about the degree of mixing in the tail. This distinction alone leads to a factor-of-two difference in the resulting F_g . On basic grounds, one expects the pressure term to modify the tail structure beyond a few ξ_0 . On the other hand, linear theory provides a good description of the far-field wake. Comparing μ or F_g predicted by the BHL model with that from linear theory therefore provides a direct test of how well BHL captures the far-field wake.

In linear theory, the (normalized) steady-state density induced by a body moving hypersonically ($\mathcal{M} \gg 1$) in a homogeneous 3D medium is given by

$$\frac{\rho}{\rho_0} = 1 + \frac{GM}{c_s^2} \frac{2}{(x^2 - \mathcal{M}^2 R^2)^{1/2}} \quad (46)$$

at the Mach cone ($x > \mathcal{M}R$), and 1 outside of it (e.g., Dokuchaev 1964; Rephaeli & Salpeter 1980; Just & Kegel 1990; Ostriker 1999). The last expression is properly valid if $x^2 - \mathcal{M}^2 R^2 \gg (GM/c_s^2)^2$, implying $x \gg \mathcal{M}\xi_0$. From Equation (46), we obtain that the column density at $x \gg \mathcal{M}\xi_0$ that contributes to the gravitational drag is

$$\mu(x) = 2\pi \int_0^{x/\mathcal{M}} (\rho - \rho_0) R dR = 4\pi\xi_0 \rho_0 x. \quad (47)$$

Therefore, linear theory predicts

$$\frac{\mu}{2\pi\rho_0\xi_0^2} = 2\tilde{x}, \quad (48)$$

whereas the BHL framework yields

$$\frac{\mu}{2\pi\rho_0\xi_0^2} \simeq \frac{\tilde{x} - \tilde{x}_0}{1 - (\tilde{x}_0/x)^{1/\tilde{x}_0}} \simeq \tilde{x} \quad (49)$$

in the far field (see bottom panel of Fig. 3 and Raga et al. 2022). Thus, for wakes much longer than $\gg \mathcal{M}\xi_0$, the BHL model underestimates the far-field gravitational drag in the homogeneous 3D case.

Now consider the limiting case of a 2D planar medium ($H \rightarrow 0$). From Equation (41) in Muto et al. (2011), linear theory predicts that the gravitational drag force exerted by the portion of the wake between $x = \mathcal{M}\xi_0$ and $x = \infty$ is $\delta F_g \simeq \pi GM\Sigma/\mathcal{M}$. In contrast, within the BHL framework, it is

$$\delta F_g = 2\sqrt{2}GM\Sigma\xi_0^{1/2} \int_{\mathcal{M}\xi_0}^{\infty} x^{-3/2} dx = 4\sqrt{\frac{2}{\mathcal{M}}} GM\Sigma \quad (50)$$

(see Section 4). Hence, for an infinite-length wake in the 2D planar case and for $\mathcal{M} = 5$, the BHL model overestimates F_g by nearly a factor of 2.

7 CONCLUDING REMARKS

In this paper, we have studied the flow structure (linear density, velocity and stagnation point position x_0), the mass accretion rate and the drag force on an accretor that moves in a straight line in the midplane of a vertically stratified environment. As in the classical BHL problem involving a homogeneous medium, we assume that the tail is sufficiently thin to be described by a one-dimensional model.

ment for model A, their result relies on a finite-box correction applied to the impact parameter, whereas it should instead be applied to the wake extent, as done here.

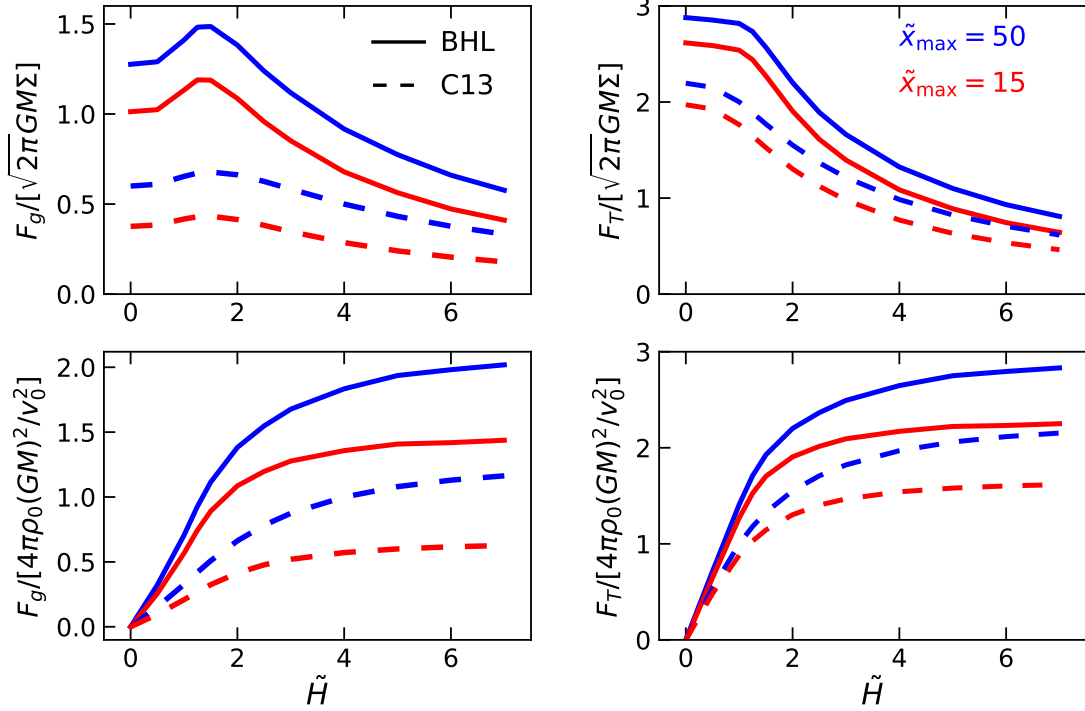


Figure 6. Gravitational drag F_g (left column) and the total drag F_T (gravitational plus accretion contributions; right column) for two different values of \tilde{x}_{\max} , as a function of \tilde{H} .

Similarly to the homogeneous case, there exist infinite solutions that satisfy the boundary conditions.

In the limit of an infinitely thin layer, we have found a simple analytical solution that satisfies conditions (I)-(VI). This analytical solution may serve as a benchmark for future studies and as a valuable reference for pedagogical purposes.

For finite thickness, the solution was obtained by performing the integration inward and employed a shooting method to identify solutions that satisfy conditions (I)-(VI) described in Section 2. This approach allowed us to determine a narrow region in the parameter space (\tilde{H}, \tilde{x}_0) where these conditions are met. Within this region, the central value of \tilde{x}_0 as a function of ξ_0 and H has been provided. The central value of \tilde{x}_0 reaches a maximum at $\tilde{H} = 1$. For such a value of \tilde{H} , and at fixed Σ , the tail is both densest and slowest. In the limit of an infinitely thick layer, we recover the BHL solution found by Matsuda et al. (2015) for a homogeneous medium.

We have also computed the accretion rate \dot{M} and derived a fitting formula. If the surface density of the layer is kept constant, the maximum accretion occurs in the case of an infinitely thin layer. If the midplane density ρ_0 is held constant and \tilde{H} is varied, \dot{M} remains approximately constant for $\tilde{H} \gtrsim 2$. We have found that \dot{M} is slightly smaller in the BHL approach than in the C11-C13 model when $H > 2\xi_0$. The values predicted by the BHL model are in good agreement with those obtained in the simulations of C13.

We have further determined the drag force due to accretion and the gravitational drag force by the part of the tail that is not being accreted. By comparing with the simulations of C13, we have found that the BHL approach underestimates the total drag force for thick layers. For thin layers ($H \leq 1.4\xi_0$), the BHL framework reproduces

the values of F_T contributed by the nonlinear part of the tail, although it is expected to overestimate the total drag when the tail becomes very long.

In addition to neglecting the pressure effects implied by the BHL assumptions, our calculations are based on further simplifying approximations. First, we neglect the curvature effects that arise when perturbers move along Keplerian orbits within discs around a massive central object. We also ignore radial density gradients in the disc. Moreover, sufficiently massive perturbers can modify both the surface density and the velocity field in the disc, leading to gaps and altered flow patterns. When gaps form, the modified profiles must be used instead of the unperturbed ones, which makes the problem significantly more difficult to handle.

ACKNOWLEDGEMENTS

The author thanks the referee for a very detailed and constructive report, and Jorge Cantó for carefully reading the manuscript.

DATA AVAILABILITY

This study does not involve the use or production of original data.

REFERENCES

Antoni, A., MacLeod, M., Ramirez-Ruiz, E. 2019, ApJ, 884, 22
 Anzer, U., Borner, G., Monaghan, J. J. 1987, A&A, 176, 235

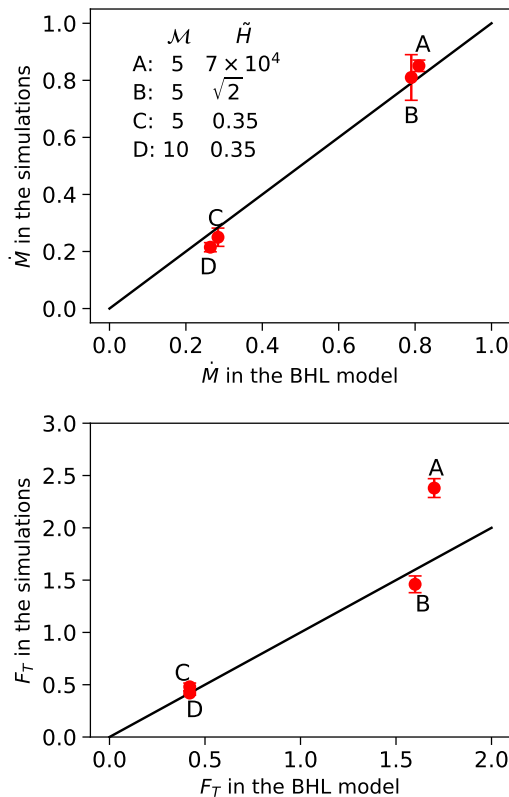


Figure 7. One-to-one comparison between the mass accretion rate \dot{M} (upper panel) and total drag force F_T (lower panel) measured in the simulations of C13 (vertical axis) and the corresponding predictions of the BHL model (horizontal axis). The solid lines represent the identity relation. \dot{M} is given in units of $\pi \rho_0 v_0 (2 \xi_0)^2$, whereas the forces are expressed in units of $4 \pi \rho_0 (GM)^2 / v_0^2$. In the upper panel, the symbols have been slightly offset horizontally to avoid overlap.

Artymowicz, P., Lin, D. N. C., Wampler, E. J. 1993, *ApJ*, 409, 592
 Beckmann, R. S., Slyz, A., Devriendt, J. 2018, *MNRAS*, 478, 995
 Bernal, C. G., Sánchez-Salcedo, F. J. 2013, *ApJ*, 775, 72
 Bisnovatyi-Kogan, G. S., Kazhdan, Ya. M., Klypin, A. A., Lutskii, A. E., Shakura, N. I. 1979, *Soviet Astronomy*, 23, 201
 Blondin, J. M. 2013, *ApJ*, 767, 135
 Bondi, H. 1952, *MNRAS*, 112, 195
 Bondi, H., Hoyle, F. 1944, *MNRAS*, 104, 273
 Burleigh, K. J., McKee, C. F., Cunningham, A. J. 2017, *MNRAS*, 468, 717
 Cantó, J., Raga, A. C., Esquivel, A., Sánchez-Salcedo, F. J. 2011, *MNRAS*, 418, 1238 (C11)
 Cantó, J., Esquivel, A., Sánchez-Salcedo, F. J., Raga, A. C. 2013, *MNRAS*, 762, 21 (C13)
 Carciofi, A. C. 2011, in Neiner C., Wade G., Meynet G., Peters G.eds, Proc. IAU Symp. 272, Active OB Stars: Structure, Evolution, Mass Loss, and Critical Limits. Cambridge University Press, Cambridge, p. 325
 Chen, Y.-X., Bailey, A., Stone, J., Zhu, Z. 2022, *ApJ*, 939, L23
 Chen, Y.-X., Jiang, Y.-F., Goodman, J. 2025, *ApJ*, 987, 188
 Choksi, N., Chiang, E., Fung, J., Zhu, Z. 2023, *MNRAS*, 525, 2806
 Ciotti, L., Pellegrini, S. 2017, *ApJ*, 848, 29
 Dittmann, A. J., Cantiello, M., Jermyn, A. S. 2021, *ApJ*, 916, 48
 Dokuchaev, V. P. 1964, *Soviet Astronomy*, 8, 23
 Edgar, R. G., 2004, *NewAR*, 48, 843

Hanuschik, R. W. 1996, *A&A*, 308, 170
 Horedt, G. P. 2000, *ApJ*, 541, 821
 Hoyle, F., & Lyttleton, R. A. 1939, *PCPS*, 35, 405
 Ida, S., Muto, T., Matsumura, S., Brasser, R. 2020, *MNRAS*, 494, 5666
 Igumenshchev, I. V., Narayan, R. 2002, *ApJ*, 566, 137
 Just, A., Kegel, W. H. 1990, *A&A*, 232, 447
 Kaaz, N., Antoni, A., Ramírez-Ruiz, E. 2019, *ApJ*, 876, 142
 Krumholz, M. R., McKee, C. F., Klein, R. I. 2006, *ApJ*, 638, 369
 Lee, A. T., Cunningham, A. J., McKee, C. F., Klein, R. I. 2014, *ApJ*, 783, 50
 Lescaudron, S., Dubois, Y., Beckmann, R. S., Volonteri, M. 2023, *A&A*, 674, A217
 Li, Y.-P., Chen, Y.-X., Lin, D. N. C. 2023, *MNRAS*, 526, 5346
 Li, Q.-C., Yang, Y.-P., Wang, F. Y., Xu, K., Shao, Y., Liu, Z.-N., Dai, Z.-G. 2021, *ApJ*, 918, L5
 Lin, D. N. C., Murray, S. D. 2007, *ApJ*, 661, 779
 Livio, M., Soker, N., de Kool, M., Savonije, G. J. 1986, *MNRAS*, 222, 235
 Lyttleton, R. A. 1972, *MNRAS*, 160, 255
 MacLeod, M., Ramírez-Ruiz, E. 2015, *ApJ*, 803, 41
 Martin, R. G., Lubow, S. H., Vallet, D., Overton, M., Lepp, S., Zhu, Z. 2025, *MNRAS*, 539, L31
 Matsuda, T., Inoue, M., Sawada, K. 1987, *MNRAS*, 227, 785
 Matsuda, T., Sekino, N., Sawada, K., Livio, M., Anzer, U., Borner, G. 1991, *A&A*, 248, 301
 Matsuda, T., Isaka, H., Ohsugi, Y. 2015, *Prog. Theor. Exp. Phys.*, 11, 113E01
 Mayer, L., Kazantzidis, S., Madau, P., Colpi, M., Quinn, T., Wadsley, J. 2007, *Science*, 316, 1874
 Muto, T., Takeuchi, T., Ida, S. 2011, *ApJ*, 737, 37
 Negueruela, I., Okazaki, A. T. 2001, *A&A*, 369, 108
 Negueruela, I., Okazaki, A. T., Fabregat, J., Coe, M. J., Munari, U., Tomov, T. 2001, *A&A*, 369, 117
 Okazaki, A. T., Bate, M. R., Ogilvie, G. I., Pringle, J. E. 2002, *MNRAS*, 337, 967
 Okazaki, A. T., Hayasaki, K., Moritani, Y. 2013, *PASJ*, 65, 41
 Ostriker, E. C. 1999, *ApJ*, 513, 252
 Papaloizou, J. C. B. 2002, *A&A*, 388, 615
 Papaloizou, J. C. B., Larwood, J. D. 2000, *MNRAS*, 315, 823
 Proga, D., Begelman M. C. 2003, *ApJ*, 582, 69
 Prust, L. J., Bildsten, L. 2024, *ApJ*, 966, 103
 Raga, A. C., Cantó, J., Castellanos-Ramírez, A., Rodríguez-González, A., Rivera-Ortiz, P. R. 2022, *Rev. Mex. Astr. Astrop.*, 58, 215
 Rein, H. 2012, *MNRAS*, 422, 3611
 Rephaeli, Y., Salpeter, E. E. 1980, *ApJ*, 240, 20
 Rosenthal, M. M., Chiang, E. I., Ginzburg, S., Murray-Clay, R. A. 2020, *MNRAS*, 498, 2054
 Ruffert, M. 1996, *A&A*, 311, 817
 Sánchez-Salcedo, F. J. 2012, *ApJ*, 745, 135
 Sánchez-Salcedo, F. J. 2019, *ApJ*, 885, 152
 Sánchez-Salcedo, F. J. 2020, *ApJ*, 897, 142
 Sánchez-Salcedo, F. J., Santillán, A., Chametla, R. O. 2018, *ApJ*, 860, 129
 Sánchez-Salcedo, F. J., Santillán, A. 2025, *MNRAS*, 537, 2647
 Sawada, K., Matsuda, T., Anzer, U., Borner, G., Livio, M. 1989, *A&A*, 221, 263
 Secunda, A., Hernandez, B., Goodman, J., Leigh, N. W. C., McKernan, B., Ford, K. E. S., Adorno, J. I. 2021, *ApJ*, 908, 27
 Soker, N. 1990, *ApJ*, 358, 545
 Suzuguchi, T., Sugimura, K., Hosokawa, T., Matsumoto, T. 2024, *ApJ*, 966, 7
 Taam, R. E., Fryxell, B. A. 1988, *ApJ*, 327, L73
 Thun, D., Kuiper, R., Schmidt, F., Kley, W. 2016, *A&A*, 589, A10
 Toropina, O. D.; Romanova, M. M.; Lovelace, R. V. E. 2012, *MNRAS*, 420, 810
 Vicente, R., Cardoso, V., Zilhão, M. 2019, *MNRAS*, 489, 5424
 Xiang-Gruess, M., Papaloizou, J. C. B. 2013, *MNRAS*, 431, 1320
 Xu, W., Stone, J. 2019, *MNRAS*, 488, 5162
 Zhou, S., Sun, M., Liu, T., Wang, J.-M., Wang, J.-X., Xue, Y. 2024, *ApJ*, 966, L9

APPENDIX A: CHARACTERISTIC TIMESCALES FOR BODIES IN ELLIPTICAL ORBITS

We consider an accretor of mass M embedded in the midplane of a protoplanetary disc around a solar-mass star, on an orbit with semi-major axis a and eccentricity e . Following [Muto et al. \(2011\)](#) (see also [Sánchez-Salcedo 2020](#)), the timescales for radial migration t_a , and eccentricity damping t_e , defined as

$$t_a \equiv \frac{a}{\langle da/dt \rangle}, \quad (\text{A1})$$

and

$$t_e \equiv \frac{e}{\langle de/dt \rangle} \quad (\text{A2})$$

can be evaluated in the local approximation. In these expressions, the angle brackets $\langle \cdot \rangle$ denote an average over one orbit. Note that, in our convention, the timescale is negative if the associated orbital element decreases with time.

To facilitate comparison with previous studies, we consider a disc with surface density $\Sigma \propto r^{-3/2}$, a constant aspect ratio h , and a disc mass of $2M_J$ (where M_J is the Jupiter mass) contained within 5 au. Figure A1 shows t_a and t_e as a function of e for a body with $a = 1$ au, and two different values of M and h . To compute the BHL total drag force, we must specify the cut-off parameter \tilde{x}_{\max} . For the case $M = 1M_{\oplus}$ and $h = 0.05$, we adopt $\tilde{x}_{\max} = 200$, whereas for $M = 67M_{\oplus}$ and $h = 0.025$, we take $\tilde{x}_{\max} = 50$. We have also plotted results using the dynamical friction force derived by [Muto et al. \(2011\)](#) (their Equation 41) based on linear theory in a 2D disc, as well as the corresponding timescales from [Papaloizou & Larwood \(2000\)](#), computed using their Equations (31) and (32). We note that [Papaloizou & Larwood \(2000\)](#) do not provide t_a directly, but instead give t_m , the timescale for changes in angular momentum. Nevertheless, t_a can be readily obtained using

$$2t_a = \left(t_m^{-1} + \frac{e^2}{1-e^2} t_e^{-1} \right)^{-1}. \quad (\text{A3})$$

For $M = 1M_{\oplus}$ and $h = 0.05$, \tilde{H} is very large ($\tilde{H} \gtrsim 150$ for $e = 0.2$ and $\tilde{H} \gtrsim 2000$ for $e = 0.75$, at all points along the orbit). Since the force increases logarithmically on \tilde{H} in both C13 and BHL, the two approaches predict very similar timescales. For $M = 67M_{\oplus}$ and $h = 0.025$, the BHL model yields slightly shorter timescales than C13. We warn, however, that for this combination of parameters the local approximation is unlikely to be a good assumption ([Sánchez-Salcedo 2019](#)).

We find that C13 and BHL predict timescales that are significantly shorter than those obtained by [Papaloizou & Larwood \(2000\)](#) and [Muto et al. \(2011\)](#) because these latter studies account only for the disc response at distances larger than $\sim H$, neglecting the contribution of the wake within the disc thickness (see also [Sánchez-Salcedo et al. 2018](#)). As a result, they effectively provide upper limits to the migration and damping timescales.

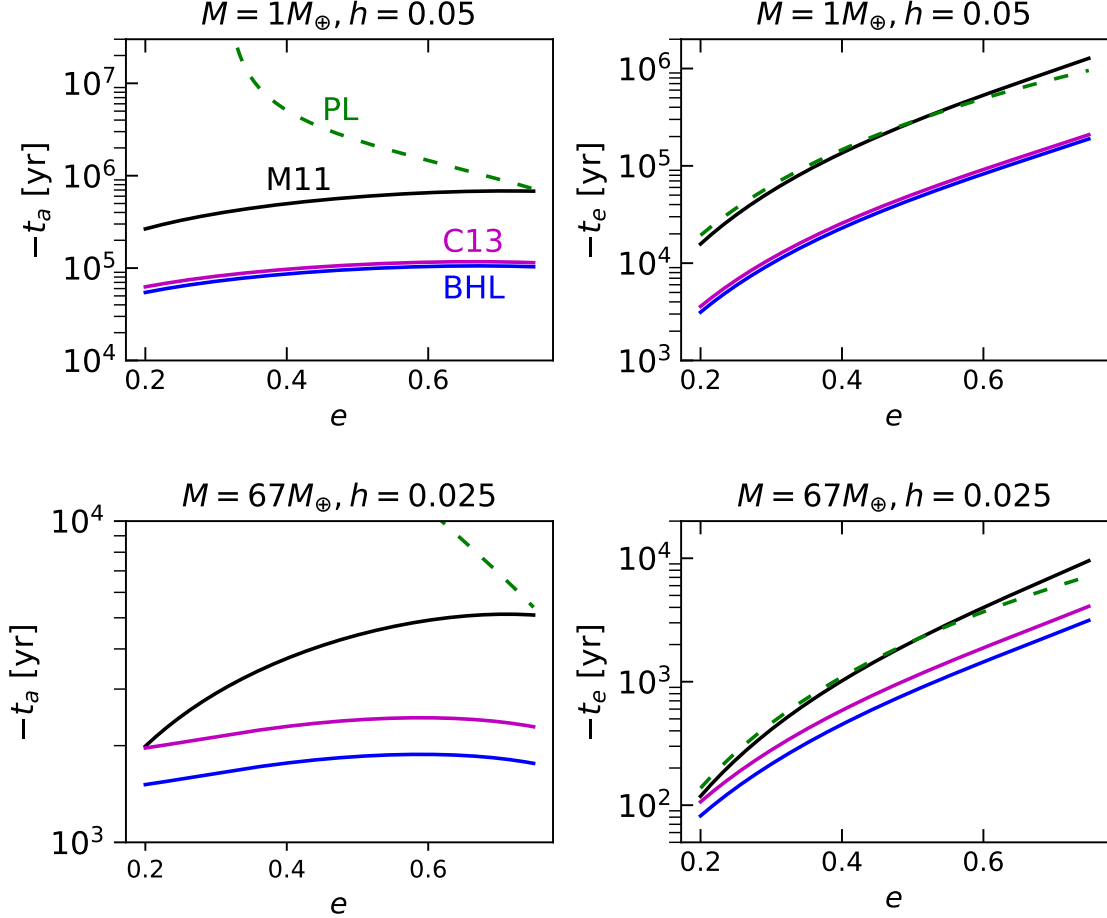


Figure A1. Radial migration timescale t_a (left column) and eccentricity damping timescale t_e (right column) as functions of eccentricity. The upper panels correspond to $M = 1M_{\oplus}$ and $h = 0.05$, while the lower panels show results for $M = 67M_{\oplus}$ and $h = 0.025$. In the upper left panel, curves are labeled according to the underlying prescription: PL denotes the model of Papaloizou & Larwood (2000), and M11 that of Muto et al. (2011). For a given set of parameters, the shortest timescales are obtained with the BHL model.